Atmos. Meas. Tech. Discuss., 5, 8189–8222, 2012
www.atmos-meas-tech-discuss.net/5/8189/2012/
doi:10.5194/amtd-5-8189-2012

Atmospheric Measurement Techniques Discussions

Improved cloud mask algorithm for FY-3A/VIRR data over the northwest region of China

X. Wang, W. Li, Y. Zhu, and B. Zhao

Laboratory for Climate and Ocean-Atmosphere Studies, Department of Atmospheric and Oceanic Sciences, School of Physics, Peking University, Beijing, 100871, China

Received: 29 August 2012 – Accepted: 30 October 2012 – Published: 6 November 2012

Correspondence to: W. Li (lwb@pku.edu.cn)

Published by Copernicus Publications on behalf of the European Geosciences Union.

Abstract

The existence of various land surfaces has always been a difficult problem for researchers who study cloud detection using satellite observations, especially over bright surfaces such as snow and desert. To improve the cloud mask result over complex terrain, an unbiased daytime cloud detection algorithm for the Visible and InfRared Radiometer (VIRR) on board the Chinese FengYun-3A polar-orbiting meteorological satellite is applied over the northwest region of China. Based on the statistical seasonal threshold tests, the algorithm consists of six main channels centered on the wavelengths of 0.63, 0.865, 10.8, 1.595, 0.455, and 1.36 μm. The combination of the unbiased algorithm and the specific threshold tests for special surfaces has effectively improved the cloud mask results over complex terrain and decreased the false identifications of clouds. The visual images over snow and desert adopting the proposed scheme exhibit better correlations with true-color images than do the VIRR official cloud mask results. The validation with the Moderate Resolution Imaging Spectroradiometer (MODIS) cloud mask product shows that the probability of detection for clear-sky regions over snow of the new scheme has increased nearly five times over the official method, and the false-alarm ratio for cloudy areas over desert has reduced by half compared with the official result. With regard to comparisons between ground measurements and cloud mask results, this approach also provides acceptable correspondence with the ground observations except for some cases, which are mainly obscured by cirrus clouds.

1 Introduction

Satellite remote sensing has always involved the significant challenge of distinguishing cloudy from clear-sky areas. The presence of clouds contaminates radiometric observations (Kidder and Vonder Haar, 1995), which may cause errors in the retrieval of atmospheric compositions and parameters, especially for research on aerosols

AMTD
5, 8189–8222, 2012

(Kaufman et al., 2005). Considering the large effect of clouds on radiance, it is necessary to provide techniques to separate clouds from clear-sky areas.

Many cloud detection algorithms have been proposed, depending on the purposes of the observations and specifications of the imager. The International Satellite Cloud Climatology Project (ISCCP) presented statistical-threshold tests for visible and infrared radiance to differentiate cloudy and clear scenes over various climate regions (Rossow, 1989; Rossow and Garder, 1993). The Advanced Very High Resolution Radiometer (AVHRR) Processing scheme Over cLouds, Land, and Ocean (APOLLO) used two visible and three infrared bands to screen clouds (Saunders and Kriebel, 1988; Gesell, 1989; Kriebel et al., 2003). Clouds from AVHRR (CLAVR) used sequential decision-threshold tree tests to identify the pixels, which were classified into 2×2 global area-coverage pixel arrays over cloud-free, mixed, and cloudy regions (Stowe et al., 1991, 1994). The dynamic threshold cloud masking (DTCM) algorithm used dynamic thresholds to screen clouds over land for AVHRR data and correctly identified a comparable or higher number of cloud-contaminated pixels compared with the CLAVR scheme (Vittorio and Emery, 2002). The cloud mask algorithm for the 36-channel Moderate Resolution Imaging Spectroradiometer (MODIS) was determined by the final confidence flags based on five groups of threshold tests (Ackerman et al., 1998). Based on the infrared trispectral algorithm, the cloud thermodynamic phase-discrimination method applied to MODIS data introduced three additional bands located at 0.65, 1.63, and 1.90 µm to improve the accuracy of phase retrieval (Baum et al., 2000). Ishida and Nakajima (2009) proposed an unbiased cloud detection scheme based on a neutral concept to restructure the final confidence flags of the MODIS cloud mask algorithm (MOD35) and applied the unbiased CLoud and Aerosol Unbiased Decision Intellectual Algorithm (CLAUDIA) to a virtual imager to investigate the efficiency of existing and future spaceborne imagers (Nakajima et al., 2011). The Visible Infrared Imager Radiometer Suite (VIIRS) cloud mask derived from the automated analysis data provided a critical data product for the NPOESS program (Hutchison et al., 2005). The cloud screening algorithm for Environmental Satellite–Medium Resolution Imaging

AMTD
5, 8189–8222, 2012

Spectrometer (ENVISAT-MERIS) multispectral imagers was based on the extraction of meaningful physical features to increase cloud detection accuracy (Gómez-Chova et al., 2007). For FengYun-3A/Visible and InfRared Radiometer (FY-3A/VIRR), the official cloud mask scheme used multiple-feature (single channel or multiple channels in combination) thresholds determined by a dynamic histogram method or forward modeling results (Yang et al., 2011). A daytime cloud detection algorithm with good performance has also recently been adopted for FY-3A/VIRR; this is an automatic daytime cloud mask technique based on the multispectral threshold synthesis method inherited from MODIS. By adding the difference between the 1.38- and 1.6-μm bands, it can provide improved results for high-cloud detection (He, 2011).

To realize accurate cloud masking results, the algorithm should also consider the potential impact of various land surfaces. Especially for brighter surfaces such as snow and desert, large reflectance similar to that of clouds could probably result in these particular clear-sky areas being classified as cloudy. Focused on improving the cloud detection over brighter surfaces, researchers have tried different methods. For discrimination of snow-covered areas, the normalized difference snow index (NDSI) has been widely used for many sensors. Defined by the two bands centered on 0.57 and 1.65 μm, NDSI was introduced for Landsat Thematic Mapper (TM) images (Dozier, 1984, 1989). For the VEGETATION (VGT) sensor, the normalized difference snow/ice index (NDSII) was proposed based on the reflectance values of red and mid-infrared spectral bands (Xiao et al., 2001). NDSI was also applied in the cloud detection algorithm of MODIS (Ackerman et al., 1998). By adding the cloud-phase identification, cloud detection over snow/ice for MODIS was developed (King et al., 2004). Relying on the 1.6-, 2.2-, and 1.38-μm-band observations from MODIS, two multispectral enhancement techniques were proposed for distinguishing between regions of cloud and snow cover (Miller et al., 2005). MODIS also added six tests to separate clouds over desert regions in daytime imagery, which include a 13.9 μm and a 6.7 μm single brightness temperature test, a 1.38 μm reflectance test, and three brightness temperature difference tests (11 minus 12 μm, 3.7 minus 11 μm, and 3.7 minus 3.9 μm) (Ackerman et al.,

AMTD
5, 8189–8222, 2012

1998). To enhance the performance of the cloud mask in the vicinity of desert areas, data from 0.4 µm was used based on the strong contrast between highly reflective clouds and less reflective cloud-free desert regions (Hutchison and Jackson, 2003). For water cover, the normalized difference vegetation index (NDVI) was an effective discrimination method. Defined by the red and near-infrared bands, NDVI was widely applied in vegetative studies (Nemani and Running, 1989; Defries and Townshend, 1994; Carlson and Ripley, 1997). For water-covered regions, the value of NDVI was always negative compared with clouds and other primary land surfaces. Based on this fact, NDVI was also adopted to discriminate water areas (Giglio et al., 2003; Lunetta et al., 2006; Gao et al., 2007).

In this paper, an unbiased daytime cloud detection algorithm based on CLAUDIA is applied to FY-3A/VIRR data over the northwest region of China. For multispectral threshold tests, it is necessary to provide a method to regroup the results of each single test to produce a final result. According to the regrouping schemes, prevailing algorithms are designed in two main categories: clear conservative (such as APOLLO and MOD35) and cloud conservative (such as ISCCP). The CLAUDIA algorithm provides a new concept to recombine the single threshold test results. It refers to the multiple threshold method employed in the MODIS cloud mask scheme but reconstructs the calculation method for the final confidence flags to realize neutral results (Ishida and Nakajima, 2009). For mixed pixels, which include clouds and surfaces, the unbiased technique does not directly identify these pixels as clouds or clear areas but calculates clear confidence levels. It provides a more accurate cloud mask result that is not biased to either clear or cloudy. Considering the advantages, the concept of the unbiased algorithm will be introduced into the cloud detection for FY-3A/VIRR in this paper to improve the official cloud mask product of VIRR over the northwest region of China. Focused on the complex terrain, specific threshold tests will be also added into the improved algorithm to mask the special clear-sky surfaces such as desert, snow, and water. The seasonal thresholds used in this paper will be calculated from statistical data for the year 2010.

AMTD
5, 8189–8222, 2012

This paper includes five sections. Section 2 describes the background and data used. Section 3 provides details of the threshold experiments and descriptions of the improved cloud mask algorithm for FY-3A/VIRR. Section 4 describes applications of the cloud mask scheme and compares them with the official products and ground observations. Finally, Sect. 5 provides a summary and discussion.

2 Background and data

2.1 Background

The existence of bright land surfaces that have similar radiative characteristics as clouds always leads to errors in cloud detection results. Over snow-covered regions, the high reflectance and cold temperature make it difficult to separate clouds from clear-sky areas. A similar problem exists when the underlying surface is desert. The cloud detection algorithm cannot only depend on the single wavelength threshold test. It is necessary to add more effective techniques to avoid false identifications. In this study, the region from 34° N to 40° N and from 73° E to 82° E, which lies in the northwest region of China, was chosen for cloud detection experiments. The complex terrain of this region (including snow/ice, desert, water, and land) always results in errors when masking clouds. In this paper, the combination of the unbiased algorithm and specific threshold tests for special surfaces has greatly improved the cloud detection results over the study region.

2.2 Data

FY-3A, China's new generation polar-orbiting meteorological satellite, is capable of a wide range of spectral detection, from ultraviolet, visible, infrared, to the microwave spectrum. It operates at the altitude of 831 km. The local time of the descending node is 10:05 UTC. An onboard sensor, VIRR, which has ten bands in the wavelengths from

AMTD
5, 8189–8222, 2012

0.44 to 12.5 µm, the scanning range of ±55.4° and a resolution of 1.1 km, is one of its key instruments (Dong et al., 2009).

In this study, six main channels of VIRR L1 (level 1) data were used for the cloud detection algorithm (Table 1). The robustness of the results was examined through comparisons with the VIRR official cloud mask product, the MODIS cloud mask product (MOD35), and ground observations from the Meteorological Information Comprehensive Analysis and Process System (MICAPS). The VIRR official cloud mask product was generated by the multiple-feature (single channel or multiple channels in combination) threshold tests determined by a dynamic histogram method or forward modeling results (Yang et al., 2011) and was provided in hierarchical data format version 5 (HDF5). Ground observations from MICAPS were also used to examine the cloud detection scheme. MICAPS is an interactive computer system that integrates all meteorological, satellite, and radar data into one computer workstation (Li et al., 2010). Version 3.0 includes 19 main categories of data (labeled as 19 diamonds); this comparison used the measurements of the total amount of clouds from the ground weather stations, as listed in diamond 1.

All of the FY-3A original data and products can be downloaded from the website of the National Satellite Meteorological Center (online at http://fy3.satellite.cma.gov.cn). MICAPS data can be obtained from Peking University (email: xyl@pku.edu.cn).

3 Methodology

The cloud detection algorithm was mainly based on the CLAUDIA algorithm, which applied the threshold method used in MOD35 but reconstructed the scheme for calculating the final confidence flag (Ishida and Nakajima, 2009; Nakajima et al., 2011). According to the channel settings of VIRR, new groups were proposed for unbiased confidence calculations, and additional steps were added for cloud discrimination over special surfaces.

AMTD
5, 8189–8222, 2012

3.1 Traditional threshold definition and tests

The thresholds used in this cloud mask algorithm were calculated according to statistical data, obtained from the original observations of VIRR onboard FY-3A during the year 2010. For this analysis, four months (January, April, July, and October) were selected to build a statistical database to represent conditions during the four different seasons. The results are presented in five different types: land, snow, water, desert, and clouds.

The traditional thresholds are determined based on the statistical results of the single channel or index. The settings of three thresholds are quite similar to those of MOD35: the low limit, the high limit, and the threshold for pass or fail (T). The low and high limits represent the minimum and maximum of the overlapping intervals, respectively. Values of T are calculated using a technique used in the research of rain areas (Lovejoy and Austin, 1979). We define a loss function f as

$$f = \frac{A_b}{A} + \frac{B_a}{B},$$

where A and B represent the real total statistical pixels of two types or categories, respectively, T is the threshold to determine which type the pixel belongs to, A_b is the number of A incorrectly classified as B according to T, and B_a is the number of B incorrectly classified as A. When the loss function f achieves a minimum such that the sum of the incorrect classified ratio reaches the lowest value, the threshold value will be defined as the final T.

3.1.1 Single reflectance tests

In the visible and near infrared regions, optically thick clouds usually have greater reflectance compared with the underlying surface; this is now used as an effective method to identify cloudy areas. The channels at 0.66 and 0.88 µm, the most common bands used in this spectral range, have exhibited good performance in cloud masking.

AMTD
5, 8189–8222, 2012

However, reflectance tests may falsely identify bright surfaces, such as deserts and snow-covered areas, as clouds. The statistical results presented here provide the reflectance distributions of the different surface types and clouds (Fig. 1).

Figure 1a illustrates the histograms of the reflectance at channel 0.66 µm. The reflectance of snow and clouds covers a broad range, while other types show a relatively intensive distribution. Figure 1b gives clear reflectance ranges covered by the five specific types and indicates where their median values lie (shown by slash marks). The large overlap between clouds and snow generally results in difficulties in distinguishing them. However, for land, desert, and water, a single reflectance value appears to maintain less overlap, so these surface types can be differentiated from clouds and snow by the threshold tests. Thus, two major categories can be identified as follows: Cloud (including clouds and snow), and Clear (all others). All single reflectance thresholds were calculated on the basis of this classification. Figure 1b also shows where the three specific thresholds are located. The two black lines represent the low and high limits. The T value is indicated by a red line.

Because it is near a strong water vapor absorption region, the band 1.38 µm test is quite effective at detecting thin cirrus clouds (Gao et al., 1993). Due to the sufficient water vapor in the lower atmosphere, the channel at 1.38 µm receives little scattered solar radiance from the surface or low-level clouds. Radiance increases when cirrus clouds are located above almost any atmospheric water vapor. Taking this into consideration, the reflectance threshold test at 1.38 µm of VIRR was used primarily to separate cirrus clouds from clear-sky areas and thick clouds. The single-reflectance thresholds used in this study are shown in Table 2.

3.1.2 NDSI and NDVI tests

To mark snow and water from their own categories, NDSI and NDVI thresholds, respectively, are used in the cloud detection algorithm. This section focuses mainly on the threshold tests of these two indices.

AMTD
5, 8189–8222, 2012

While the reflectance of snow cover and clouds are very similar at wavelengths below about 1 µm, they diverge in the near infrared and achieve a maximum difference at wavelengths between about 1.55 and 1.75 µm (Gareth, 2006). Based on this fact, the normalized difference snow index (NDSI) was proposed and developed for the discrimination of snow (Dozier, 1984, 1989). Here, the NDSI used for VIRR is defined as

$$\mathrm{NDSI} = \frac{r_1 - r_6}{r_1 + r_6},$$

where r_1 and r_6 are the reflectance at channels 1 (0.58–0.68 µm) and 6 (1.55–1.64 µm). The statistical histogram shows that snow and clouds could be distinctly separated by NDSI (Fig. 2a). Compared with clouds, snow typically has higher NDSI values, corresponding to the radiative properties of snow. Table 3 lists specific thresholds.

The Normalized Difference Vegetation Index (NDVI) is defined with the radiance measured by two bands in the red and near infrared as

$$\mathrm{NDVI} = \frac{r_2 - r_1}{r_2 + r_1},$$

where r_1 and r_2 are the reflectances in channels 1 (0.58–0.68 µm) and 2 (0.84–0.89 µm). Figure 2b illustrates the distribution of NDVI. Because the reflectance of the visible channel is greater than that of the near-infrared channel, the NDVI values for water are negative. For land or desert, NDVI values are greater than or around zero; this difference can be used to mask water regions. Table 3 provides the thresholds for different seasons. For April, because there was no overlap between water and the other types in its category, the pixels covered with water could be picked up only by the value of the low limit.

3.2 Linear threshold definition and tests

To pick up the residual cloudy pixels over the bright desert, channel 7 (0.43–0.48 µm) and channel 4 (10.3–11.3 µm) are used simultaneously in the algorithm. For the

AMTD
5, 8189–8222, 2012

wavelength at channel 7, there is a strong contrast between the more highly reflective clouds and the less reflective cloud-free desert. Combined with channel 4, where the cloud has a lower brightness temperature than clear sky, this contrast separates cloudy pixels from bright desert surfaces.

Figure 3 shows the scatter diagrams for the combined use of these two channels. The cloudy pixels can be clearly discriminated from the clear surfaces, especially from the bright desert. According to the distribution in Fig. 3, a linear threshold is introduced to discriminate the residual cloudy pixels from the clear category. The linear form is determined by two factors: the slope and the intercept. As mentioned in Sect. 3.1, when the loss function f achieves a minimum, the line defined by the two factors is chosen to be the final linear threshold. Figure 3 and Table 4 show the linear thresholds and the loss function values for different seasons.

3.3 Cloud detection algorithm

3.3.1 Unbiased confidence flag

CLAUDIA classifies individual tests into two groups based on the trend observed in each test, which is distinct from other prevailing approaches of classification based on the wavelength domain or the primary target of each test (Ishida and Nakajima, 2009). This study used the CLAUDIA classification. To realize unbiased cloud detection, two groups needed to be formed: tests that prefer to be clear conservative (Group 1), and tests that exhibit trends of being cloudy-conservative (Group 2). The rules for classifying individual tests were based on the method proposed by Ishida and Nakajima (2009). According to this method, the single threshold tests of VIRR can be divided into two groups: Group 1 (clear conservative) includes the channels 1 and 2 reflectance tests; and Group 2 contains only the reflectance test for channel 10.

The definitions of individual confidence levels for single tests used in this study are similar to those used in MOD35 (Fig. 4). The method for calculating the three thresholds has been described above (see Sect. 3.1). When the observed values are higher than

AMTD
5, 8189–8222, 2012

the high limit (or lower than the low limit), probably due to clear sky, the confidence level is assigned to be 1, whereas, if the observed levels are lower than the low limit (or higher than the high limit), with cloudy properties, the confidence level is recorded at 0. The confidence level is set at 0.5 when the observation equals the value of T, determined by the loss function. Observations between the low and high limits are divided into two parts: higher than T or lower; the confidence level is also calculated by two linear functions.

The final confidence flags are determined by the equations proposed in CLAUDIA, which are quite different from MOD35:

$$Q_1 = 1 - \sqrt{(1-q_1)(1-q_2)}$$

$$Q_2 = q_{10}$$

$$Q_{\text{final}} = \sqrt{Q_1 Q_2}$$

where q_1, q_2, and q_{10} represent the values of individual confidence levels at channels 1, 2, and 10, respectively, Q_1 and Q_2 are the values of confidence level for groups 1 and 2, and Q_{final} is the final confidence flag.

Unlike MOD35, which divides pixels into four levels (clear, probably clear, uncertain, cloudy), the confidence levels of ambiguous pixels can be defined between 0 and 1 based on the unbiased algorithm, making the selection of the pixels for specific research targets easier.

When finishing these steps, the pixels can be divided into the two categories defined above: Cloud or Clear types (see Sect. 3.1.1).

3.3.2 Special surface mask

Three specific tests are used for cloud screening over special surfaces: NDSI, NDVI, and combined two-channel tests. Based on the values of the final confidence level, the pixels are classified into two categories: Cloud types (Q_{final} between 0 and 0.5) and Clear types (Q_{final} between 0.5 and 1). The pixels included in the Cloud category are

AMTD
5, 8189–8222, 2012

selected for the NDSI test, and the remaining pixels transfer to the other two tests. The flow chart (Fig. 5) gives the specific process of the improved cloud detection algorithm. The pixels could be selected by the T value, when it exists; otherwise, the value of the low limit (or high limit) would be used.

4 Cloud mask results and comparisons

4.1 Comparison with official cloud mask product and MOD35

This section focuses on the validation of the proposed algorithm over complex terrain by visual image inspection and by comparisons with the VIRR official cloud mask product and the MODIS cloud mask product (MOD35). The MOD35 and the VIRR official cloud mask product contains four confidence levels: high confidence of clouds (cloudy), low confidence of clouds (uncertain), low confidence of clear-sky (probably clear), and high confidence of clear-sky (clear). The new cloud mask result provides the specific value of confidence level for each pixel, except pixels covered with water, snow, and residual clouds over desert. For comparison, the new cloud mask image is also divided into four levels by the value of the final confidence level: above 0.75 (clear), between 0.5 and 0.75 (probably clear), between 0.25 and 0.5 (uncertain), and less than 0.25 (cloudy).

Figure 6 shows the cloud mask result over the desert region located from 37.6° N to 40° N and from 77.6° E to 80.8° E. Data were obtained on 6 March 2011, at 05:25 UTC. Figure 6a is the gray image of VIRR channel 4 (10.3–11.3 µm). Figure 6b is the true-color VIRR image composed of channel 1 (red), channel 9 (green), and channel 7 (blue). Figure 6c is the new cloud mask result obtained from the algorithm proposed in this study. Figure 6d is the VIRR official cloud mask product image. Compared with the VIRR official cloud mask product, the new cloud algorithm is in good agreement with the infrared image and the true-color image. The new cloud mask scheme gives more accurate areas covered by clouds, especially for the cloud located at the left bottom of the image. By applying the two-channel linear threshold test, the residual

AMTD
5, 8189–8222, 2012

clouds (labeled as light blue) have been detected, greatly improving the cloud mask result over the bright desert. Apparently, the official cloud mask result overestimates the amount of clouds, and cannot provide the specific distributions of clouds.

To provide a specific validation, the MODIS cloud mask product (MOD35), as a high-quality cloud mask product, is taken as "truth" for the validation of the proposed cloud mask algorithm. Two indices are applied to the comparison with MOD35: the probability of detection (POD) and the false-alarm ratio (FAR). These two statistical indices, which are widely used to evaluate the precipitation detection results (Cheng and Brown, 1995; Behrangi et al., 2010), could be adopted to estimate the accuracy of the improved cloud mask results. The definitions in this study are as below:

$$\mathrm{POD} = H/(H+M)$$
$$\mathrm{FAR} = F/(H+F).$$

The specific representation of each parameter is shown in Fig. 7. For comparison, the data of MOD35 for the desert case were obtained on 6 March 2011, at 05:25 UTC. In order to eliminate the differences between the spatial resolutions of MODIS and VIRR, the distances between the pixels from these two sensors are calculated as below

$$S = 2 \times 6378.137 \arcsin\sqrt{\sin^2\frac{a}{2} + \cos^2(\mathrm{lat}_1)\cos^2(\mathrm{lat}_2)\sin^2\frac{b}{2}}$$
$$a = \mathrm{lat}_1 - \mathrm{lat}_2$$
$$b = \mathrm{lon}_1 - \mathrm{lon}_2,$$

where S represents the distance between two pixels, lat_1, lat_2, lon_1, and lon_2 are the latitudes and longitudes of two pixels, respectively. The minimum distance is then applied to collocate MODIS with VIRR. However, the distance should not exceed 1 km.

Focused on the cloudy pixels for the case over desert, the values of POD for the new cloud mask scheme and the VIRR official cloud mask product are 53.261 % and 67.217 %, achieving similar accuracy. However, the values of FAR have been greatly improved from 14.499 % (VIRR official cloud mask) to 6.998 % (the new cloud mask).

AMTD
5, 8189–8222, 2012

Figure 6e illustrates the MOD35 cloud mask image of the case over desert. One of the reasons that the POD of the proposed cloud mask scheme is slightly lower than that of the official product is probably because of the false identifications of the special terrain in the bottom right corner of the image by MOD35. Figure 6f shows the true-color image of VIRR over the same region on a different date. It is obvious that the area in the bottom right corner is supposed to be clear-sky pixels. However, the pixels in this area were falsely identified as cloudy ones in MOD35 and the official product of VIRR, which resulted in a slightly lower POD value for the proposed scheme.

Figure 8 shows a scene over a snow-covered region from 34.6° N to 37° N and from 74.5° E to 77.7° E, on 22 January 2011 at 05:45 UTC. Figure 8a is the VIRR gray image of channel 6 (1.55–1.64 µm). The settings of the other three images are the same as in Fig. 6. The difference between the reflectance of snow cover and clouds achieves a maximum at wavelengths between about 1.55 and 1.75 µm, and snow shows a lower reflectance (Gareth, 2006). According to this result, the dark-colored areas in Fig. 8a could probably be classified as snow-covered regions. Combined with the true-color image, it is apparent that this region is largely covered by snow. Compared with the VIRR official cloud mask product, the new cloud detection algorithm has greatly improved the result over the snow-covered region. The snow-covered areas (shown in yellow), which should be masked as clear, have been modified by the new cloud mask scheme. The official product provides incorrect distributions of clouds and underestimates the areas of clear sky. This could probably introduce errors into subsequent research.

The data from MOD35 on 22 January 2011 at 05:45 UTC as "truth" are applied for the comparison of the case over snow. Focused on the clear-sky pixels, the values of FAR for the new cloud mask scheme and the VIRR official cloud mask product are at a similar level of accuracy with values of 43.345 and 32.485 %, respectively. However, the values of POD have been greatly increased from 15.659 % (VIRR official cloud mask) to 71.743 % (the new cloud mask). Figure 8e shows the MOD35 cloud mask image of the case over snow. Compared with MOD35, the identifications of clear-sky

AMTD
5, 8189–8222, 2012

pixels have been dramatically improved by the proposed scheme over snow-covered regions, especially for the area in the bottom left corner of the image.

4.2 Comparison with MICAPS observation

Ground observations from MICAPS can also be compared with the cloud detection results. Two weather stations located in the research region are used for comparisons: the Hetian site (79.93° E, 37.13° N), and the Bachu site (78.57° E, 39.8° N). The total amount of clouds observed at these weather stations, which is presented as the ratio of clouds in the naked-eye observed sky, can be used for the validation. According to the rules of ground measurement, if the average height of the clouds is 4 km and the angle of view is 10°, the area for cloud observation covers approximately 1617 km^2 (Malberg, 1973). Thus, for the cloud detection image, the percentage of clouds is calculated in the region centered at the weather station with a radius of 22.7 km. Based on the pass time of FY-3A, the ground observations at 14:00 LT are used for the validation. Table 5 lists the comparisons.

Compared with the observations at the weather stations, the new cloud mask results provide basically good correlations except several cases where the estimated amount of clouds is generally smaller than the ground observations. For ground observations, the curvature of the Earth may result in overestimation of low clouds with a small horizontal angle because openings between clouds can be overlooked; for satellite observations, the presence of thin cirrus clouds may result in underestimation due to the poor identification of them in space (Malberg, 1973). Figure 9 shows the two cases with poor correlations centered on the Hetian site with a 4° × 4° array. For the case on 21 January, the infrared image (Fig. 9a) clearly reveals that Hetian site was covered by cirrus clouds. By adding the linear threshold test, parts of the residual cirrus clouds over desert have been screened out, but the proposed cloud mask scheme still underestimates the amount of cirrus clouds. For the case on 16 February the high thin cirrus clouds located to the southeast of the site are not identified by the new algorithm. The similar cold temperature and high reflectance make it difficult to discriminate

AMTD
5, 8189–8222, 2012

the thin cirrus clouds over the northwest region of China using only the infrared and near-infrared wavelengths.

5 Conclusions

This study developed an unbiased daytime cloud detection algorithm for FY3A/VIRR. Based on statistical seasonal threshold tests, six main channels were adopted to improve the cloud mask over the northwest region of China. Focused on the complex terrain, the combination of the unbiased algorithm and the specific threshold tests for special surfaces has greatly improved the cloud detection result, especially for the regions covered by snow and desert. By comparison of the visual images, the results from the new cloud mask scheme are highly consistent with the true-color images. For the comparison with MOD35, the new cloud scheme shows almost five times as much POD as does the VIRR official cloud mask result over snow, and it reduces FAR over the desert region by half.

Observations from MICAPS were also used to examine the cloud mask technique. The new cloud mask results were relatively well correlated except for several cases, which were attributed primarily to the poor detection of cirrus clouds. Because the detection of cirrus clouds continues to be a difficult problem in cloud masking, more effective methods or channels should to be examined in future research to improve cloud mask results.

Acknowledgements. This work was supported by the National Natural Science Foundation of China (No. 40921160380).

AMTD
5, 8189–8222, 2012

References

Ackerman, S. A., Strabala, K. I., Menzel, W. P., Frey, R. A., Moeller, C. C., and Gumley, L. E.: Discriminating clear sky from clouds with MODIS, J. Geophys. Res., 103, 32141–32157, 1998.

Baum, B. A., Soulen, P. F., Strabala, K. I., King, M. D., Ackerman, S. A., Menzel, W. P., and Yang, P.: Remote sensing of cloud properties using MODIS airborne simulator imagery during SUCCESS 2. Cloud thermodynamic phase, J. Geophys. Res., 105, 11781–11792, 2000.

Behrangi, A., Hsu, K., Imam, B., and Sorooshian, S.: Daytime precipitation estimation using bispectral cloud classification system, J. Appl. Meteorol. Clim., 49, 1015–1031, 2010.

Carlson, T. N. and Ripley, D. A.: On the relation between NDVI, fractional vegetation cover, and leaf area index, Remote Sens. Environ., 62, 241–252, 1997.

Cheng, M. and Brown, R.: Delineation of precipitation areas by correlation of Meteosat visible and infrared data with radar data, Mon. Weather Rev., 123, 2743–2757, 1995.

Defries, R. S. and Townshend, J. R. G.: NDVI-derived land cover classifications at a global scale, Int. J. Remote Sens., 15, 3567–3586, 1994.

Dong, C., Yang, J.,Zhang, W., Yang, Z., Lu, N., Shi, J., Zhang, P., Liu, Y., and Cai, B.: An overview of a new Chinese weather satellite FY-3A, B. Am. Meteorol. Soc., 90, 1531–1544, 2009.

Dozier, J.: Snow reflectance from Landsat-4 thematic mapper, IEEE T. Geosci. Remote, GE-22, 323–328, 1984.

Dozier, J.: Spectral signature of alpine snow cover from the landsat thematic mapper, Remote Sens. Environ., 28, 9–22, 1989.

Gómez-Chova, L., Camps-Valls, G., Calpe-Maravilla, J., Guanter, L., and Moreno, J.: Cloud-screening algorithm for ENVISAT/MERIS multispectral images, IEEE T. Geosci. Remote, 45, 4105–4118, 2007.

Gao, B.-C., Goetz, A. F. H., and Wiscombe, W. J.: Cirrus cloud detection from airborne imaging spectrometer data using the 1.38 µm water vapor band, Geophys. Res. Lett., 20, 301–304, doi:10.1029/93GL00106, 1993.

Gao, B.-C., Montes, M. J., Li, R.-R., Dierssen, H. M., and Davis, C. O.: An atmospheric correction algorithm for remote sensing of bright coastal waters using MODIS land and ocean channels in the solar spectral region, IEEE T. Geosci. Remote, 45, 1835–1843, 2007.

Gareth, R. W.: Remote Sensing of Snow and Ice, CRC Press, Boca Raton, 285 pp., 2006.

AMTD
5, 8189–8222, 2012

Gesell, G.: An algorithm for snow and ice detection using AVHRR data An extension to the APOLLO software package, Int. J. Remote Sens., 10, 897–905, 1989.
Giglio, L., Descloitres, J., Justice, C. O., and Kaufman, Y. J.: An enhanced contextual fire detection algorithm for MODIS, Remote Sens. Environ., 87, 273–282, 2003.
He, Q.-J.: A daytime cloud detection algorithm for FY-3A/VIRR data, Int. J. Remote Sens., 32, 6811–6822, 2011.
Hutchison, K. D. and Jackson, J. M.: Cloud detection over desert regions using the 412 nanometer MODIS channel, Geophys. Res. Lett., 30, 2187, doi:10.1029/2003GL018446, 2003.
Hutchison, K. D., Roskovensky, J. K., Jackson, J. M., Heidinger, A. K., Kopp, T. J., Pavolonis, M. J., and Frey, R.: Automated cloud detection and classification of data collected by the Visible Infrared Imager Radiometer Suite (VIIRS), Int. J. Remote Sens., 26, 4681–4706, 2005.
Ishida, H. and Nakajima, T. Y.: Development of an unbiased cloud detection algorithm for a spaceborne multispectral imager, J. Geophys. Res., 114, D07206, doi:10.1029/2008JD010710, 2009.
Kaufman, Y. J., Remer, L. A., Tanre, D., Li, R.-R., Kleidman, R., Mattoo, S., Levy, R. C., Eck, T. F., Holben, B. N., Ichoku, C., Martins, J. V., and Koren, I.: A critical examination of the residual cloud contamination and diurnal sampling effects on MODIS estimates of aerosol over ocean, IEEE T. Geosci. Remote, 43, 2886–2897, 2005.
Kidder, S. Q. and Haar, T. H. V.: Satellite Meteorology: an Introduction, Academic Press, California, 466 pp., 1995.
King, M. D., Platnick, S., Yang, P., Arnold, G. T., Gray, M. A., Riedi, J. C., Ackerman, S. A., and Liou, K.-N.: Remote sensing of liquid water and ice cloud optical thickness and effective radius in the Arctic: application of airborne multispectral MAS data, J. Atmos. Ocean. Tech., 21, 857–875, 2004.
Kriebel, K. T., Gesell, G., Kästner, M., and Mannstein, H.: The cloud analysis tool APOLLO: improvements and validations, Int. J. Remote Sens., 24, 2389–2408, 2003.
Li, Y., Cao, L., Gao, S., and Lu, B.: The current stage and development of MICAPS, Meteor. Mon., 36, 50–55, 2010.
Lovejoy, S. and Austin, G. L.: The delineation of rain areas from visible and IR satellite data for GATE and mid-latitudes, Atmos. Ocean, 17, 77–92, 1979.

AMTD
5, 8189–8222, 2012

Lunetta, R. S., Knight, J. F., Ediriwickrema, J., Lyon, J. G., and Worthy, L. D.: Land-cover change detection using multi-temporal MODIS NDVI data, Remote Sens. Environ., 105, 142–154, 2006.
Malberg, H.: Comparison of mean cloud cover obtained by satellite photographs and ground-based observations over Europe and the Atlantic, Mon. Weather Rev., 101, 893–897, 1973.
Miller, S. D., Lee, T. F., and Fennimore, R. L.: Satellite-based imagery techniques for daytime cloud/snow delineation from MODIS, J. Appl. Meteorol., 44, 987–997, 2005.
Nakajima, T., Tsuchiya, T., Ishida, H., Matsui, T., and Shimoda, H.: Cloud detection performance of spaceborne visible-to-infrared multispectral imagers, Appl. Optics, 50, 2601–2616, 2011.
Nemani, R. R. and Running, S. W.: Estimation of regional surface resistance to evapotranspiration from NDVI and thermal-IR AVHRR data, J. Appl. Meteorol., 28, 276–284, 1989.
Rossow, W. B.: Measuring cloud properties from space: a review, J. Climate, 2, 201–213, 1989.
Rossow, W. B. and Garder, L. C.: Cloud detection using satellite measurements of infrared and visible radiances for ISCCP, J. Climate, 6, 2341–2369, 1993.
Saunders, R. W. and Kriebel, K. T.: An improved method for detecting clear sky and cloudy radiances from AVHRR data, Int. J. Remote Sens., 9, 123–150, 1988.
Stowe, L. L., McClain, E. P., Carey, R., Pellegrino, P., Gutman, G. G., Davis, P., Long, C., and Hart, S.: Global distribution of cloud cover derived from NOAA/AVHRR operational satellite data, Adv. Space Res., 11, 51–54, 1991.
Stowe, L. L., Vemury, S. K., and Rao, A. V.: AVHRR clear-sky radiation data sets at NOAA/NESDIS, Adv. Space Res., 14, 113–116, 1994.
Vittorio, A. V. D. and Emery, W. J.: An automated, dynamic threshold cloud-masking algorithm for daytime AVHRR images over land, IEEE T. Geosci. Remote, 40, 1682–1694, 2002.
Xiao, X., Shen, Z., and Qin, X.: Assessing the potential of VEGETATION sensor data for mapping snow and ice cover: a normalized difference snow and ice index, Int. J. Remote Sens., 22, 2479–2487, 2001.
Yang, J., Dong, C., Lu, N., Yang, Z., Shi, J., Zhang, P., Liu, Y., and Cai, B.: The new generation FengYun polar-orbiting meteorological satellite of China: operational products and applications, Science Press, Beijing, 368 pp., 2011.

AMTD
5, 8189–8222, 2012

Table 1. VIRR Channels used for the cloud detection algorithm in this study.

Channel	Wavelength (μm)	Primary use
1	0.58–0.68	Cloud/surface
2	0.84–0.89	Cloud/surface
4	10.3–11.3	Cloud/surface
6	1.55–1.64	Cloud/snow
7	0.43–0.48	Cloud/surface
10	1.325–1.395	Cirrus cloud

AMTD
5, 8189–8222, 2012

Table 2. Threshold values of each single reflectance test during the four seasons.

Channel	Wavelength (μm)	Month	Low limit (%)	High limit (%)	*T* (%)	Loss function
1	0.58–0.68	Jan	8.06580	19.34070	16.07099	0.08320
		Apr	10.66770	35.44770	25.53573	0.10756
		Jul	11.41110	32.10240	28.37796	0.09233
		Oct	14.26080	25.65960	20.41618	0.02886
2	0.84–0.89	Jan	6.57140	24.35960	19.73466	0.09884
		Apr	17.91460	40.08540	29.88685	0.12845
		Jul	10.69620	40.08540	32.73809	0.10705
		Oct	15.85220	31.96470	25.68084	0.06487
10	1.325–1.395	Jan	5.83847	34.18231	23.12820	0.17885
		Apr	10.62262	46.90996	31.66926	0.14353
		Jul	8.81728	50.15957	30.72872	0.20359
		Oct	12.33770	53.31892	19.71432	0.27033

AMTD
5, 8189–8222, 2012

Table 3. Threshold values of NDVI and NDSI tests during the four seasons.

Test	Month	Low limit	High limit	T	Loss function
NDVI	Jan	−0.27090	−0.24456	−0.27090	0.01923
	Apr	−0.12216	−0.01322		
	Jul	−0.22387	0.10374	−0.01420	0.02740
	Oct	−0.15437	0.02718	−0.04726	0.00151
NDSI	Jan	0.24712	0.77336	0.61549	0.09735
	Apr	0.14484	0.70123	0.58439	0.26589
	Jul	0.12627	0.73872	0.67135	0.13091
	Oct	0.08245	0.85194	0.47489	0.15634

AMTD
5, 8189–8222, 2012

Table 4. The definition values of the linear threshold test during the four seasons.

Test	Month	Slope	Intercept	Loss function
Linear threshold test	Jan	3.0	232.0	0.04430
	Apr	0.0	270.0	0.03393
	Jul	6.0	166.0	0.07534
	Oct	3.0	238.0	0.00131

AMTD
5, 8189–8222, 2012

Table 5. Comparisons between ground observations and VIRR cloud mask results.

Time (mmdd UTC)	Hetian site percentage of clouds (%)	Cloud mask percentage of clouds (%)	Bachu site percentage of clouds (%)	Cloud mask percentage of clouds (%)
0105 05:55	0	0	70	81
0110 06:00	0	0	0	0
0121 05:55	70	16	0	0
0126 06:00	0	0	0	0
0131 06:05	70	100	70	100
0205 06:10	40	29	70	90
0216 06:05	50	0	40	32
0221 06:10	0	0	70	86
0222 05:50	70	100	70	92
0309 06:10	0	0	0	0
0310 05:50	0	0	0	0
0315 05:55	90	20	70	51

AMTD
5, 8189–8222, 2012

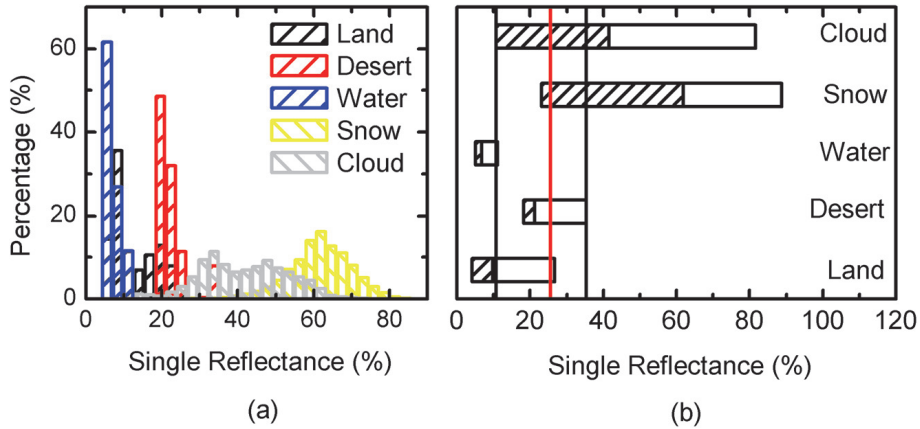

Fig. 1. (a) Histograms and **(b)** ranges of the reflectance distributions of the different surface types and clouds at channel 1 of VIRR during April in 2010; For **(b)** the location of the median values labeled as slash marks, the low limit and high limit labeled as black lines, *T* labeled as red line.

AMTD
5, 8189–8222, 2012

Improved cloud mask algorithm for FY-3A/VIRR data

X. Wang et al.

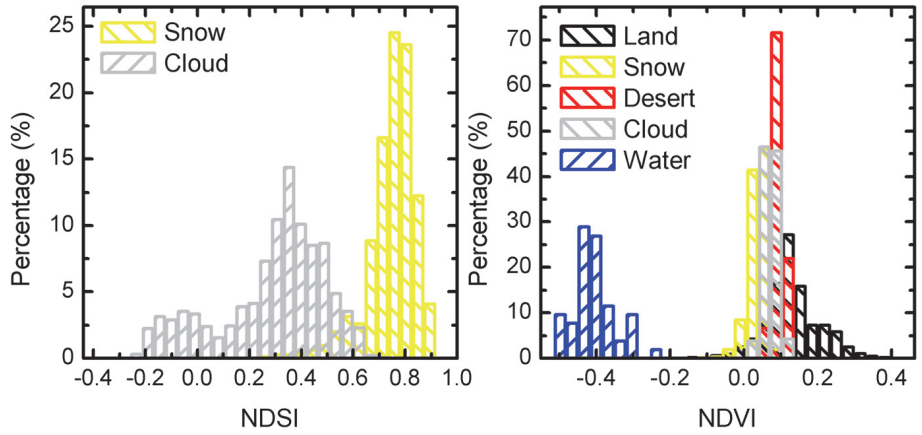

Fig. 2. Histograms of **(a)** NDSI and **(b)** NDVI distributions during January in 2010.

AMTD
5, 8189–8222, 2012

Improved cloud mask algorithm for FY-3A/VIRR data

X. Wang et al.

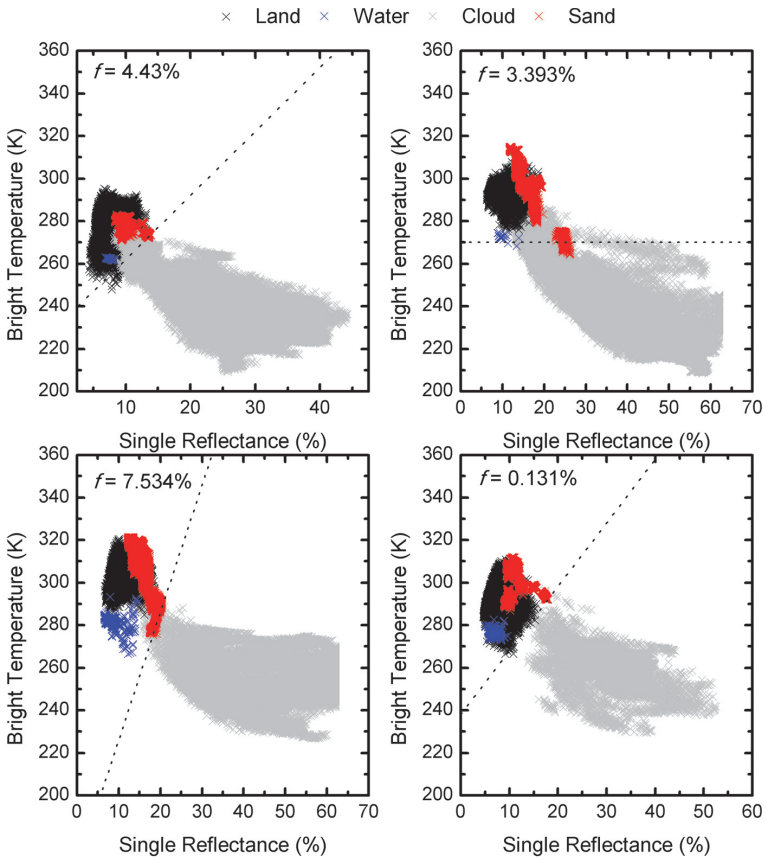

Fig. 3. The scatter diagrams for channel 4 and 7 during the four seasons; the linear thresholds (dashed lines).

AMTD
5, 8189–8222, 2012

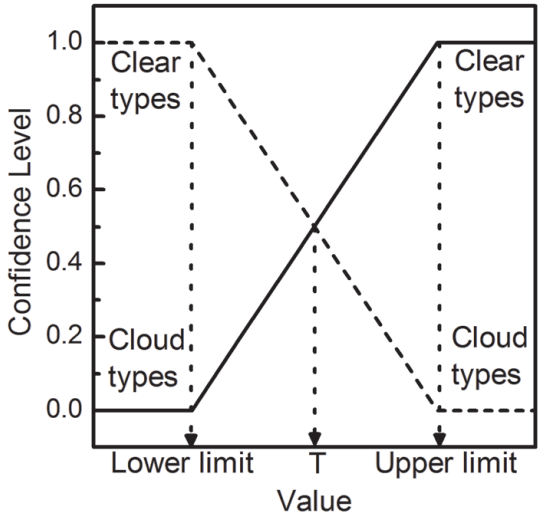

Fig. 4. Concept of the confidence levels with three threshold values.

AMTD
5, 8189–8222, 2012

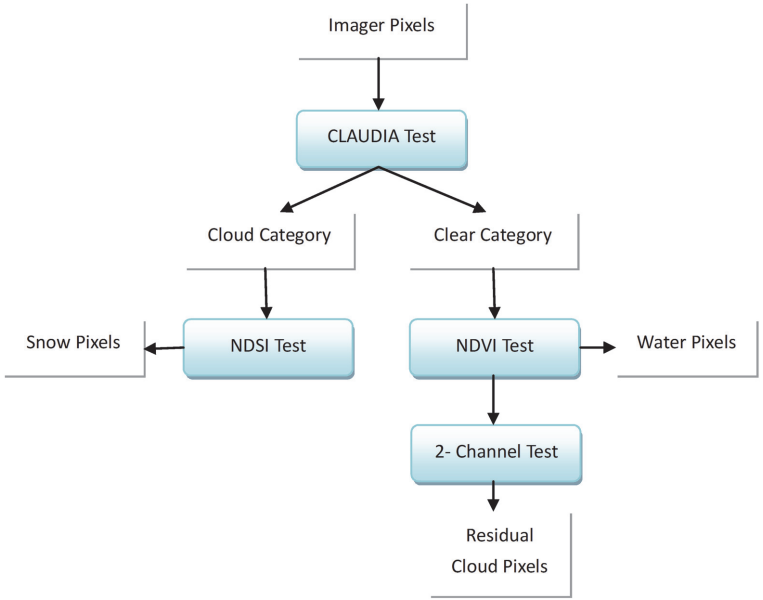

Fig. 5. The flow chart of the improved cloud detection algorithm.

AMTD
5, 8189–8222, 2012

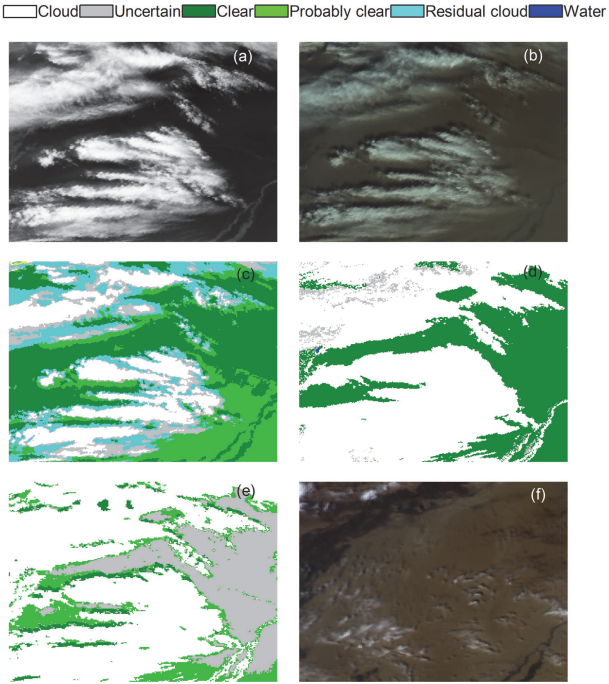

Fig. 6. The case over desert on 6 March 2011, at 05:25 UTC. **(a)** the gray image of VIRR channel 4 (10.3–11.3 μm); **(b)** the true-color VIRR image composed of channel 1 (red), channel 9 (green), and channel 7 (blue); **(c)** the new cloud mask result from the algorithm proposed in this study; **(d)** the official cloud mask product image from VIRR; **(e)** the cloud mask product image from MODIS; **(f)** the true-color VIRR image for the same region over desert on 19 August 2011, at 04:55 UTC.

AMTD
5, 8189–8222, 2012

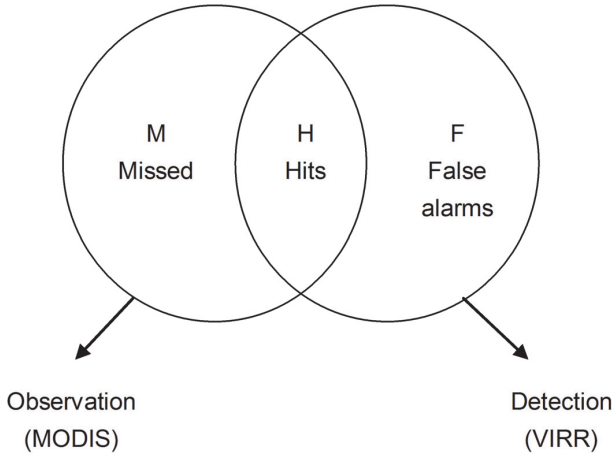

Fig. 7. The parameters of POD and FAR.

AMTD
5, 8189–8222, 2012

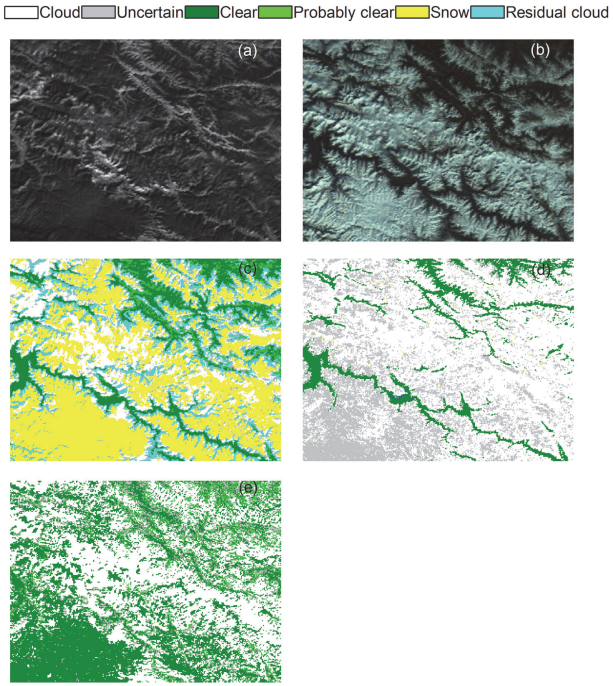

Fig. 8. The case over snow-covered region on 22 January 2011 at 05:45 UTC. **(a)** the gray image of VIRR channel 6 (1.55–1.64 µm); **(b)** the true-color VIRR image composed of channel 1 (red), channel 9 (green), and channel 7 (blue); **(c)** the new cloud mask result from the algorithm proposed in this study; **(d)** the official cloud mask product image from VIRR; **(e)** the cloud mask product image from MODIS.

AMTD
5, 8189–8222, 2012

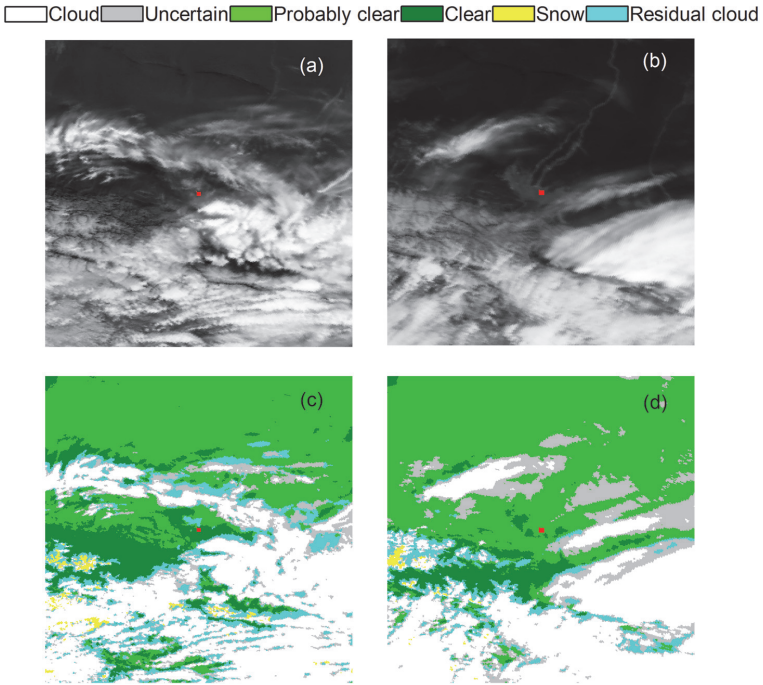

Fig. 9. The cases for comparisons at Hetian site. The red rectangle represents Hetian site; the grey image of VIRR channel 4 (10.3–11.3 μm) **(a)** on 21 January 2011 at 05:55 UTC and **(b)** on 16 February 2011 at 06:05 UTC; **(c)** and **(d)** the corresponding cloud mask results obtained from the algorithm proposed in this study.

AMTD
5, 8189–8222, 2012